Nanostructured Metal/Carbon Hybrids for Electrocatalysis by Direct Carbonization of Inverse Micelle Multilayers

Yu Jin Jang,[†] Yoon Hee Jang,[†] Sang-Beom Han,[‡] Dibyendu Khatua,[§] Claudia Hess,[⊥] Hyungju Ahn,[#] Du Yeol Ryu,[#] Kwanwoo Shin,[§] Kyung-Won Park,[‡] Martin Steinhart,[⊥] and Dong Ha Kim[†,*]

[†]Department of Chemistry and Nano Science, Ewha Womans University, 52 Ewhayeodae-gil, Seodaemun-gu, Seoul 120-750, South Korea, [‡]Department of Chemical and Environmental Engineering, Soongsil University, 511 Sangdo-dong, Dongjak-gu, Seoul 156-743, South Korea, [§]Department of Chemistry, Sogang University, Shinsoo-dong, Mapo-gu, Seoul 121-742, South Korea, [⊥]Institute of Chemistry of New Materials, Universität Osnabrück, Barabarastrasse 7, D-46069, Osnabrück, Germany, and [#]Department of Chemical and Biomolecular Engineering, Yonsei University, 50 Yonsei-ro, Seodaemun-gu, Seoul 120-749, South Korea

ABSTRACT A synthetic strategy for the fabrication of graphitic carbon nanomaterials containing highly dispersed arrays of metal nanoparticles is reported. This synthetic strategy involves successive deposition of inverse micelle monolayers containing a metal precursor and reduction of the latter, followed by direct carbonization of the obtained multilayer structure of inverse micelles containing metal nanoparticles. Thus, a "direct-carbonization" concept, in which the block copolymer simultaneously serves as soft template and as carbon source, was combined with a multilayer buildup protocol. The inner architecture of the multilayer structures consisting of carbon and metal nanoparticles was studied by X-ray reflectivity, grazing incidence small-angle X-ray scattering, and cross-sectional transmission electron microscopy imaging. The hexagonal near ordering of the metal nanoparticles in the block copolymer micelle multilayers was by and large conserved after carbonization. The resulting carbon structures containing multilayers of highly dispersed metal nanoparticles exhibit superior electrocatalytic activity in formic acid and methanol oxidation, suggesting that they are promising electrode materials for fuel cells.

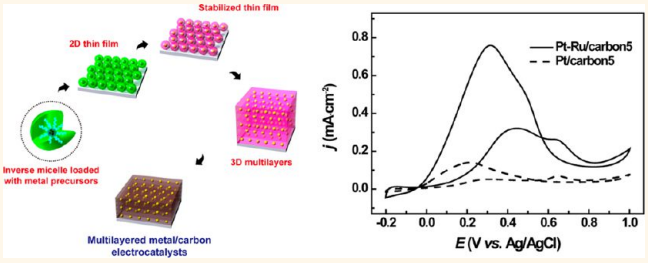

KEYWORDS: metal/carbon hybrids · direct carbonization · electrodes · self-assembly · block copolymers

The application of nanostructured carbonaceous materials exhibiting high electrical conductivity, such as graphitic carbon nanofibers,[1,2] hollow carbon capsules,[3] ordered porous carbons,[4,5] graphenes,[6] and fullerenes[7,8] as support or scaffold for catalysis, energy conversion,[9] and energy storage[10] has attracted considerable interest. Their electrocatalytic performance could be improved by their structural optimization.[11−13] Dispersion of metal catalysts, such as Pt or Pt−Ru alloy nanoparticles, on carbon scaffolds was reported to be a particularly efficient strategy to this end.[3,4] Here we report the direct carbonization of self-assembled multilayers of inverse block copolymer (BCP) micelles loaded with noble metal nanoparticles (NPs). The BCP serves as soft template in the synthesis of the NPs and, simultaneously, as carbon source. Thus, metal/carbon hybrids, which contain multilayers of dispersed metal nanoparticles in a carbon matrix, are obtained as a novel type of electrode material. The electrocatalytic performance of the metal/carbon hybrids was evaluated using formic acid oxidation and methanol oxidation as model reactions.

BCPs self-assemble into nanoscopic domain structures[14] and have been exploited as soft templates in the generation of arrays of inorganic nanoobjects.[15−19] Moreover, BCPs have gained increasing interest as a carbon source.[20−25] Recently, we generated two-dimensional graphitic carbon films containing incorporated metal nanoparticles by direct carbonization of UV-light stabilized polystyrene-*block*-poly(4-vinyl pyridine)

* Address correspondence to dhkim@ewha.ac.kr.

Received for review November 19, 2012 and accepted December 27, 2012.

Published online December 27, 2012
10.1021/nn3056115

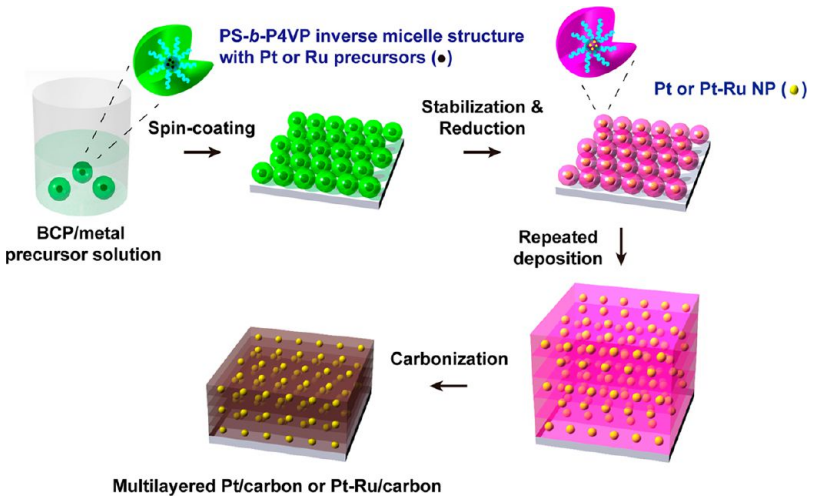

Scheme 1. Schematic diagram of the fabrication process of the metal/carbon nanostructures.

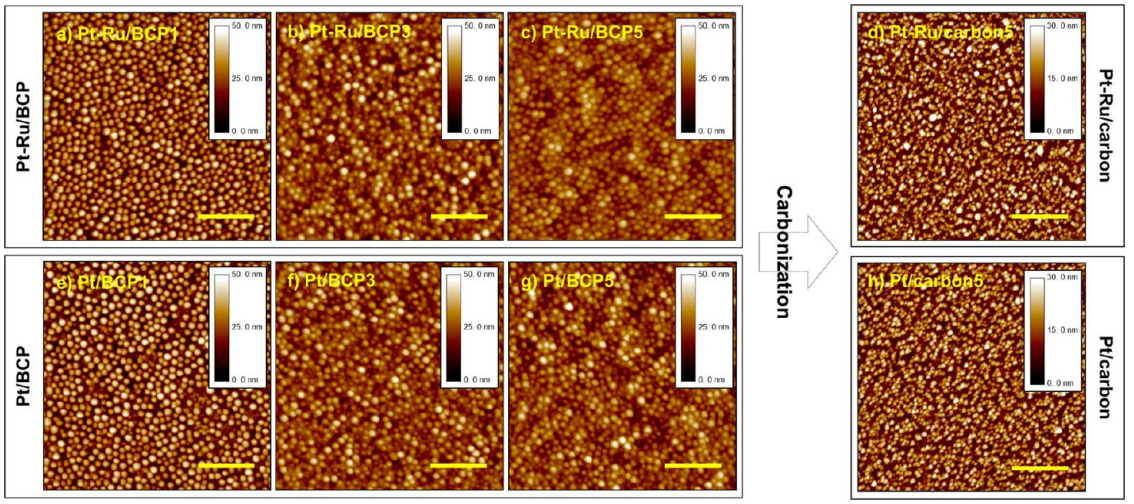

Figure 1. Height contrast AFM images of the surfaces of (a) Pt–Ru/BCP1, (b) Pt–Ru/BCP3, (c) Pt–Ru/BCP5, and (d) the carbonized counterpart of Pt–Ru/BCP5, Pt–Ru/carbon5. In the second row, height contrast AFM images of the surfaces of (e) Pt/BCP1, (f) Pt/BCP3, (g) Pt/BCP5, and (h) Pt/carbon5, the carbonized counterpart of Pt/BCP5, are seen. The scale bars in the images correspond to 500 nm.

(PS-*b*-P4VP) inverse micellar films.[26,27] The self-assembled nanoscopic structure of inverse BCP micelle layers stabilized by cross-linking with UV light could be conserved upon carbonization so that nanopatterned carbon films were obtained.[25,26] In this work, we prepared multilayered metal/carbon hybrid nanostructures containing platinum (Pt)/ruthenium (Ru) alloy NPs (Pt–Ru/carbon) or Pt NPs (Pt/carbon), as displayed in Scheme 1, by combining a layer-by-layer deposition process yielding self-ordered multilayer structures of BCP inverse micelles containing dispersed metal NPs with direct BCP carbonization. Homogeneous solutions containing PS-*b*-P4VP and metal precursor ($PtCl_4$ and/or $RuCl_3$) were spin-coated onto solid substrates so that layers of inverse BCP micelles formed (step 1). The polar metal precursors segregated to the likewise polar P4VP domains. The reverse BCP micelle layers were stabilized by cross-linking with UV light, and reduction of the metal precursors yielded metal NPs in place of the P4VP domains (step 2). Repetition of steps 1 and 2 resulted in the formation of inverse BCP micelle multilayers loaded with metal (step 3). Finally, direct carbonization of the BCP at 873 K for 1 h under Ar atmosphere without addition of further carbon sources yielded metal/carbon hybrid nanostructures.

RESULTS AND DISCUSSION

Atomic force microscopy (AFM) revealed that the quasi-hexagonal morphology of the reverse micellar monolayers was conserved upon cross-linking with UV light and reduction of the metal precursors even after the fifth deposition step (Figure 1). The surface roughness of metal/BCP samples slightly decreased after each consecutive deposition cycle. However, the change was marginal compared to the increase in total

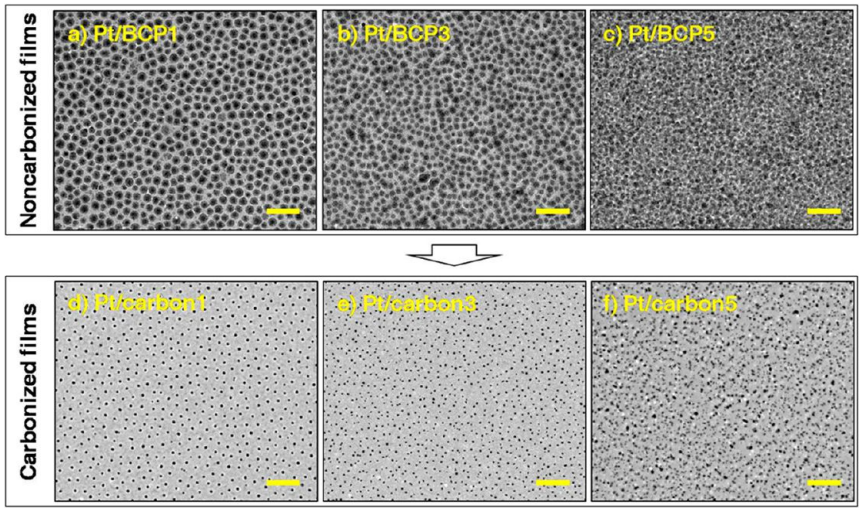

Figure 2. Top view TEM images of samples (a) Pt/BCP1, (b) Pt/BCP3, and (c) Pt/BCP5, and of their carbonized counterparts (d) Pt/carbon1, (e) Pt/carbon3, and (f) Pt/carbon5. The scale bars in the images correspond to 200 nm.

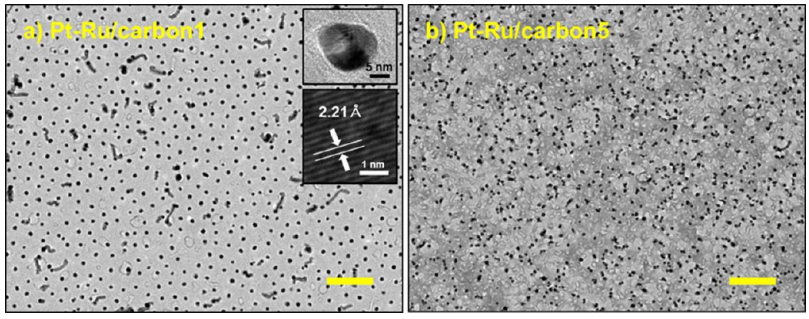

Figure 3. Top view TEM images of (a) Pt–Ru/carbon1 and (b) Pt–Ru/carbon5. The insets in panel a show a Pt-Ru NP (upper inset) and a HRTEM image of a Pt-Ru NP (lower inset). The scale bars in the images correspond to 200 nm. The worm-like features in panel a originate from the carbon coating in the preparation stage of the specimen.

film thickness per deposition cycle, as verified by X-ray reflectivity (XR) (see below) and AFM topography measurements (Supporting Information, Figure S1 and Table S1). Figure 2 displays transmission electron microscopy (TEM) images of Pt/BCP hybrid films prior to carbonization containing one (Pt/BCP1), three (Pt/BCP3), and five (Pt/BCP5) inverse micelle layers as well as of the carbonized products Pt/carbon1, Pt/carbon2, and Pt/carbon5. The Pt NPs of sample Pt/BCP1 seen as dark spots in Figure 2a were arranged in a hexagonal array, proving that their positions corresponded to those of the P4VP/$PtCl_4$ cores in the inverse micelles prior to the reduction of the $PtCl_4$. Direct comparison of the morphologies of sample Pt/BCP1 (Figure 2a) and its carbonized counterpart (Figure 2d) revealed that local hexagonal ordering was conserved upon carbonization. However, the diameter of the dark spots marking the areas containing Pt decreased from ~25 nm, (consistent with a previous report[28]) to ~15 nm, indicating that ripening in the course of the high-temperature treatment converted small Pt clusters dispersed throughout the P4VP domains into single Pt NPs. The average center-to-center distance between neighboring Pt NPs of sample Pt/carbon1 amounted to ~60 nm, as determined by image analysis. TEM images of samples Pt–Ru/carbon1 and Pt–Ru/carbon5 are shown in Figure 3. The results of high-resolution transmission electron microscopy (HRTEM) of Pt-Ru alloy NPs (Figure 3a, inset) were consistent with X-ray diffraction, which will be discussed later. Successive deposition of inverse BCP micelle monolayers containing metal NPs led to increasing numbers and higher apparent area densities of the Pt or Pt–Ru NPs in top view TEM images (Supporting Information, Figure S2 and Table S2). The number of NPs that can be separated from the brighter background (carbon) by thresholding in an imaged area of 4.3 μm^2 increases from 591 in Figure 2d (sample Pt/carbon1) to 1116 in Figure 2e (sample Pt/carbon3) to 2019 in Figure 2f (sample Pt/carbon5). Thus, the apparent area densities of the Pt NPs increased from 137 NPs/μm^2 for sample Pt/carbon1 to 260 NPs/μm^2 for sample Pt/carbon3 to 470 NPs/μm^2 for sample Pt/carbon5. It should be noted that in samples Pt/carbon3 and Pt/carbon5 individual NPs located in different layers at laterally similar positions

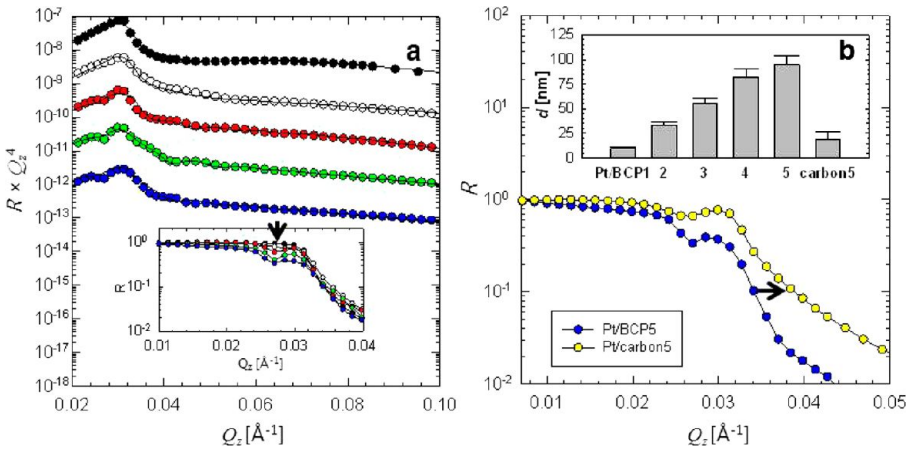

Figure 4. (a) XR data of samples Pt/BCP1 (solid black circles), Pt/BCP2 (black open circles), Pt/BCP3 (red circles), Pt/BCP4 (green circles), and Pt/BCP5 (blue circles). The reflectivities were normalized by multiplying with Q_z^4, and offset by a factor of 10. Solid lines are fits obtained by the iteration of thickness and electron density. The inset shows reflectivity curves near the critical edge without the normalization. (b) XR data of before and after the carbonization of Pt/PCB5. The arrow indicates the pronounced increase in reflected intensity after the carbonization. The inset shows thickness (d) values obtained from XR fits.

may not be separable in top view TEM images showing two-dimensional projections of the three-dimensional NP multilayer structure. Hence, NPs located in different layers at laterally similar positions may be counted as single entities. In the imaged area of Figure 3b showing sample Pt−Ru/carbon5, 1479 individual entities (344 NPs/μm^2) corresponding to single NPs or NPs with similar lateral position in different layers counted as single entities could be identified.

X-ray reflectivity (XR) measurements of samples Pt/BCP1 to Pt/BCP5 deposited onto Si substrates yielded specular XR intensity profiles (Figure 4a). As detailed in the experimental section, a critical wave vector transfer $Q_{z,c}$ is given by $4\pi/\lambda \cdot \sin\theta_c$. The critical angle θ_c can be approximated by $\theta_c \approx (2\delta)^{1/2}$, and λ is the wavelength of the incident beam. The position of $Q_{z,c}$ is directly correlated to the electron density ρ_{el} of the probed sample. The dispersion, δ, which is the real part of the index of refraction, is given by $\delta = \lambda^2\rho_{el}r_o/2\pi$, where r_o is the classical electron radius (2.82×10^{-13} cm). Most XR curves exhibited faint interference fringes, implying a certain degree of surface roughness as the reflected beams were significantly diffused out. The curve of sample Pt/BCP1 showed a broad oscillation with a period ΔQ_z indicating the presence of a monolayer of inverse micelles. For samples Pt/BCPn (n = 2, 3, 4, and 5) the frequencies of the oscillations became abruptly narrower and were shifted to lower Q_z values, indicating an increase in film thickness with increasing number of deposition cycles. A small dip below the critical edge ($Q_{z,c} \approx 0.03177$ Å^{-1}) of the Si substrate progressively appeared (Figure 4a, inset). The dip became more pronounced as the number of deposited Pt/BCP layers increased, indicating the successive increase in thickness of the inverse BCP micelle multilayer structures (that have lower electron density than the Si substrate).

XR measurements of sample Pt/carbon5 revealed a pronounced shift of the reflection intensity as compared to the XR profiles of sample Pt/BCP5 (Figure 4b). This outcome indicates significant densification and smoothening in the course of carbonization, which is accompanied by significant reduction in film thickness. Film thickness values for samples Pt/BCPn (n = 2, 3, 4, and 5) and Pt/carbon5 obtained by data fitting are shown in the inset of Figure 4b. The repeated Pt/BCP depositions resulted in stepwise, linear increase of the film thickness. The thickness of the Pt/BCP1 monolayers was calculated to be about 9.8 ± 1 nm, which is slightly thinner than the value expected for a 2-dimensional micellar PS-*b*-P4VP monolayer. However, the inverse micelle layer in direct contact with the Si substrate might exhibit an asymmetrically deformed hemimicellar structure. Although surface roughness was evident in the case of thicker films (Pt/BCP2−4), systemically varying higher frequencies of the Kiessig fringes and the deepened critical edge for the polymer layers correspond to a stepwise thickness increment of 24 ± 2.6 nm. Carbonization of sample Pt/BCP5 with a thickness of 95 ± 2 nm led to a significant decrease in thickness to 18 ± 4 nm (Figure 4b) accompanied by a drastic increase (~14%) in electron density.

The internal structures of the metal/BCP and metal/carbon multilayers were probed by two-dimensional grazing incidence small-angle X-ray scattering (2D-GISAXS) (see Supporting Information, Figure S3 for the scattering geometry). The in-plane component q_y and the out-of-plane component q_z of the scattering vector are correlated to structural features along the normal to the plane of incidence (*xz*-plane or film plane) and along the normal to the film surface, respectively. Figure 5a shows 2D-GISAXS patterns of samples Pt/BCP5 and Pt−Ru/BCP5 on Si substrates. For both samples two in-plane scattering peaks were observed

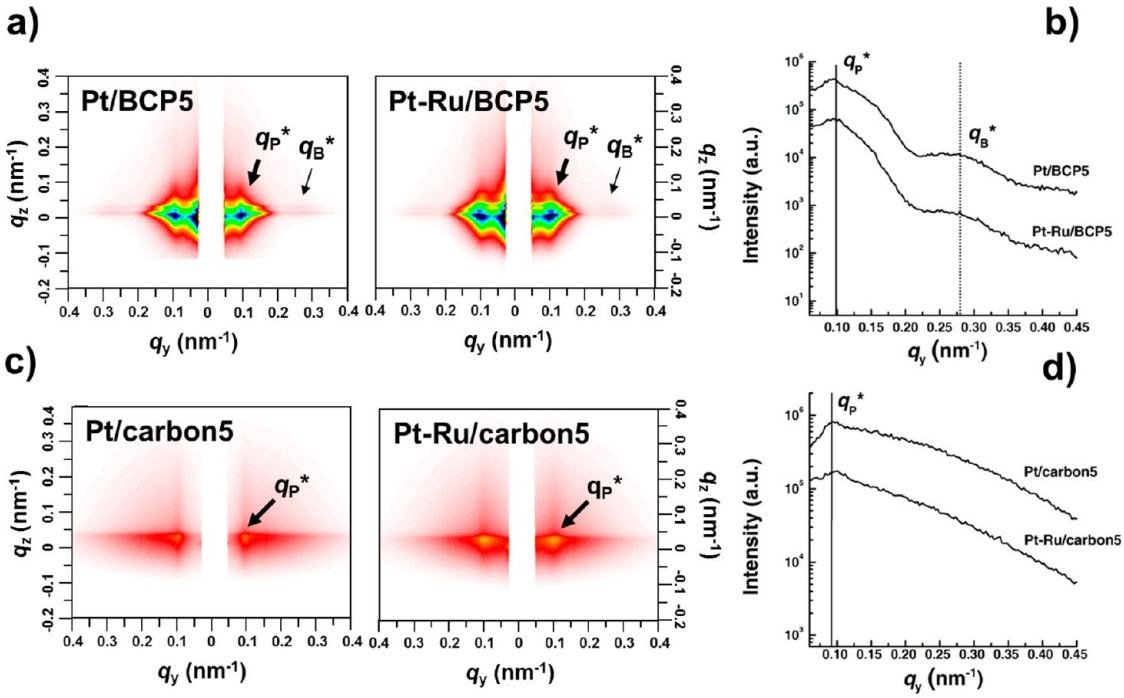

Figure 5. 2D-GISAXS patterns at an incidence angle of 0.2° to probe the internal film structure. (a) Pt/BCP5 (left) and Pt−Ru/BCP5 (right); (c) Pt/carbon5 (left) and Pt−Ru/carbon5 (right) on Si substrates. The in-plane scattering intensity profiles seen in panels b and d are line scans from the 2D-GISAXS patterns parallel to the *y*-axis (Supporting Information, Figure S3) taken near $q_z = 0$. To avoid overlapping, the in-plane scattering intensity profiles are vertically shifted by a factor of 5.

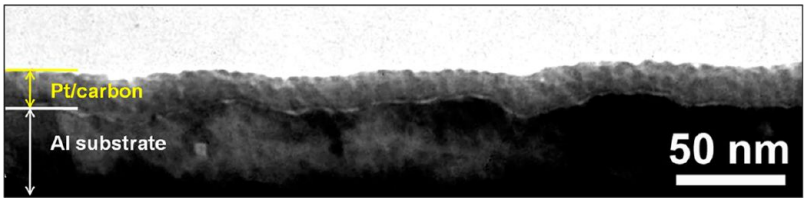

Figure 6. Cross-sectional TEM image of a Pt/carbon10 film deposited on an Al substrate.

near $q_z = 0$ (Figure 5b). The first in-plane peak at low q_y designated by a thick arrow, q_P* = 0.095 nm^{-1} (d = 66 nm), indicates that the spatial arrangement of the metal-loaded cores of the inverse micelles is characterized by pronounced near order. The broad in-plane peak at high q_y designated by a thin arrow, q_B* = 0.28 nm^{-1} (d = 22.4 nm), originates from the internal structure of the inverse metal/BCP micelles and reflects the layer sequence PS shell-metal/PVP core-PS shell. Figure 5c shows 2D-GISAXS patterns of samples Pt/carbon5 and Pt−Ru/carbon5. As obvious from the in-plane scattering intensity profile (Figure 5d), the low-q_y peak q_P* = 0.095 nm^{-1} remained at the same position as prior to the carbonization, indicating that the spatial distribution of metal has remained unaltered. The striking disappearance of the high-q_y peak q_B* can be interpreted as a signature of the complete conversion of BCP into carbon during high temperature treatment.

2D-GISAXS patterns of samples Pt/BCP5 and Pt−Ru/BCP5 (Supporting Information, Figure S4) as well as of samples Pt/carbon5 and Pt−Ru/carbon5 (Supporting Information, Figure S5) on Si substrates were measured at different incidence angles between 0.14° and 0.22°. In all 2D-GISAXS patterns, that is, for any incidence angle, the low-q in-plane scattering peak indicative of near ordering of the metal NPs was found. Thus, the uniform and near-ordered arrangement of the metal NPs is also evident along the direction perpendicular to the film plane before and after carbonization. This outcome is in line with the cross-sectional TEM image of a Pt/carbon10 film located on an Al substrate shown in Figure 6. The Pt/carbon10 film contains condensed spherical entities originating from the BCP micelles that consist of Pt NPs surrounded by densified carbon. As discussed above, carbonization of BCP inverse micelle multilayers is accompanied by significant volume shrinkage. The thickness of sample Pt/BCP10 apparent from the TEM image seen in Figure 6 was ~20 nm. The preparation of the TEM specimen by ultramicrotomy was accompanied by significant distortion of the Pt/BCP10 layer and the underlying Al

substrate. Since the thickness of one single carbonized BCP inverse micelle monolayer was around 7 nm,[25] and XR yielded a thickness of sample Pt/BCP5 of 18 ± 4 nm, we assume that the layer thickness of carbonized BCP inverse micelle multilayers does not linearly depend on the number of BCP inverse micelle multilayers.

X-ray diffraction (Figure 7) of bulk Pt/carbon confirmed the presence of fcc Pt. A slight shift of the characteristic reflections in the X-ray pattern of bulk Pt−Ru/carbon to higher 2θ angles as compared to the Pt/carbon pattern and the absence of the characteristic peaks of metallic Ru indicate that bimetallic NPs consisting of Pt−Ru alloy were obtained.[29] The alloy formation was further confirmed by X-ray photoelectron spectroscopy (XPS) (Figure 8 and Supporting Information, Table S3); as compared with Pt/carbon5, the 4*f* binding energy of Pt−Ru/carbon5 was clearly shifted to higher values. Energy-dispersive X-ray spectroscopy (EDS) revealed a Pt:Ru ratio of ~75:25 in Pt−Ru/carbon5 (Supporting Information, Figure S6). The Raman spectra of bulk Pt−Ru/carbon and Pt/carbon show *D* bands at about 1360 cm^{-1} and *G* bands at about 1600 cm^{-1}, indicating that partially graphitic carbon was formed according to Ferrari-Robertson scheme (Figure 9).[30]

The electrochemical properties of Pt−Ru/carbon5 and Pt/carbon5 were measured by cyclic voltammetry (CV) in N_2-saturated $HClO_4$ solution (Figure 10a). Both samples showed typical hydrogen adsorption/desorption behavior. However, in the presence of Ru the voltammetric profile is broader and less confined. The potential of Pt−Ru/carbon5 and Pt/carbon5 as electrodes in fuel cells was evaluated using oxidation of formic acid and methanol as model reactions. CV profiles of Pt−Ru/carbon5 and Pt/carbon5 for formic acid oxidation are displayed in Figure 10b. The onset potential of Pt−Ru/carbon was similar to that of Pt/carbon and Pt−Ru alloy did not exhibit lower peak potentials than Pt/carbon. The peak potential of sample Pt/carbon5 was ~0.3 V (*vs* Ag/AgCl). Compared with state-of-the-art Pt/carbon catalyst E-TEK,[31] the peak potential of Pt/carbon5 was shifted in positive direction. However, it was similar or shifted in negative direction compared with other homemade Pt/carbon samples.[32,33] For this reason, we compared the ratios of the peak current densities of the first (I_f) and the

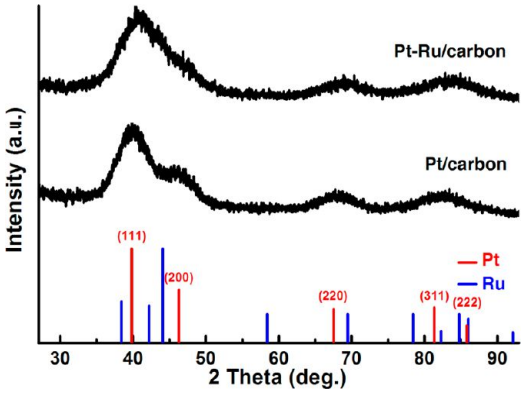

Figure 7. XRD patterns of bulk Pt−Ru/carbon (top) and bulk Pt/carbon (middle); at the bottom, calculated diffraction patterns of fcc Pt (red lines, JCPDS no. 04-0802) and hcp Ru (blue lines, JCPDS no. 06-0663) are displayed.

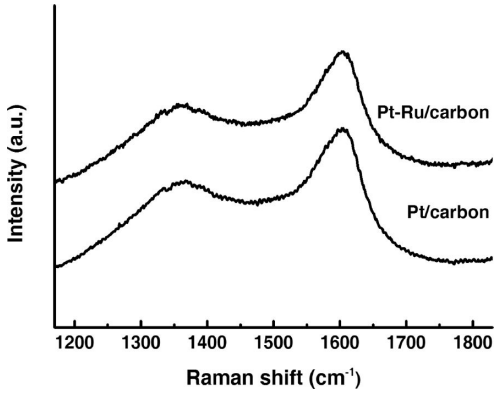

Figure 9. Raman spectra of bulk Pt−Ru/carbon (top) and bulk Pt/carbon (bottom).

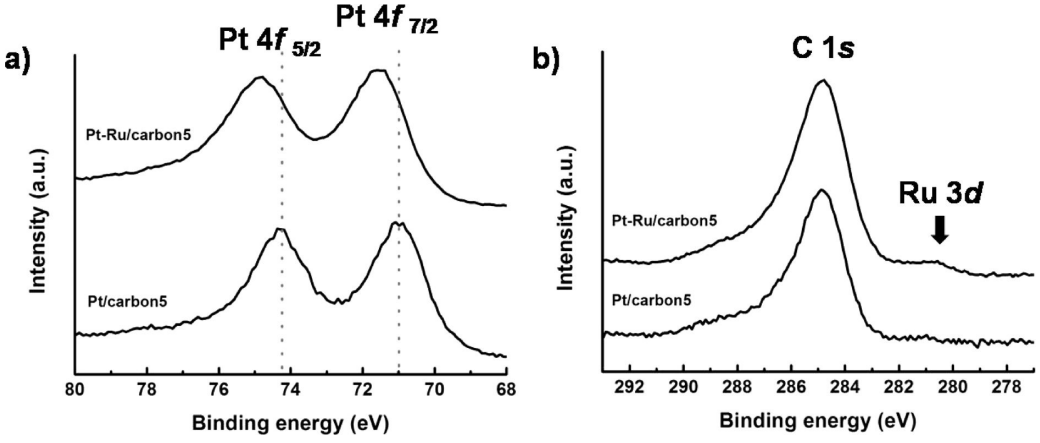

Figure 8. High resolution XPS spectra of Pt−Ru/carbon5 and Pt/carbon5: (a) Pt 4*f* region and (b) Ru 3*d* region.

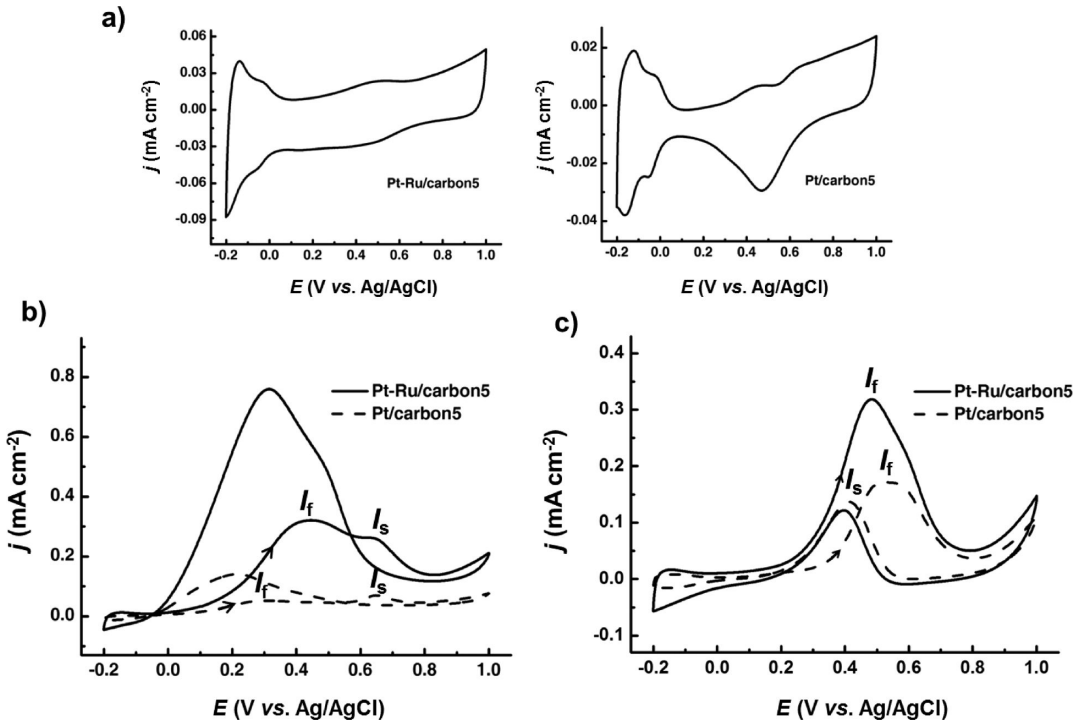

Figure 10. Cyclic voltammograms of metal/carbon5 films in N_2-saturated aqueous solutions of (a) 0.1 M $HClO_4$, (b) 0.2 M HCOOH + 0.1 M $HClO_4$, and (c) 0.2 M CH_3OH + 0.1 M $HClO_4$ at room temperature. Arrows in panels b and c indicate the direction of forward scans. The scan rate was 50 mV s^{-1}.

second anodic peak (I_s) in forward scans I_f/I_s as well as the absolute peak current densities to comparatively assess the electrocatalytic activities of the tested samples. The anodic peak current density of Pt–Ru/carbon5 was approximately four times higher than that of Pt/carbon5. This outcome is in line with previous reports according to which Pt–Ru shows electrocatalytic activity for formic acid oxidation[34–37] and introduction of Ru improves the catalytic activity of Pt.[36,37] The higher I_f/I_s value of Pt–Ru/carbon5 (I_f/I_s = 1.23) as compared to that of Pt/carbon5 (I_f/I_s = 0.736) implies that the presence of Ru enhances the tolerance of the Pt–Ru/carbon5 against CO;[32,33] formic acid is apparently directly oxidized to CO_2 by dehydrogenation, whereas dehydration of formic acid producing carbon monoxide (CO) as intermediate poisoning the catalyst is suppressed.[32] The I_f/I_s ratio of a commercial Pt/carbon catalyst (E-TEK) calculated for comparison is 0.182[31] and, therefore, significantly lower than the values obtained for Pt–Ru/carbon5 and Pt/carbon5. We also found enhanced electrocatalytic activity of Pt–Ru/carbon5 and Pt/carbon5 for methanol oxidation (Figure 10c). As compared to Pt/carbon5, the onset and peak potentials of Pt–Ru/carbon5 in the forward sweep were enhanced and the anodic peak current density of Pt–Ru/carbon5 was approximately doubled. Most importantly, the I_f/I_s ratio of Pt–Ru/carbon5 (I_f/I_s = 2.62) was markedly increased as compared to the corresponding values of Pt/carbon5 (I_f/I_s = 1.24) and of E-TEK catalyst (I_f/I_s= 0.74). This outcome can be explained by adsorbed hydroxyl species (–OH) on Ru, which are formed as a result of the dissociation of H_2O. These hydroxyl species promote the oxidation process of methanol by transfer of their oxygen to adjacent Pt atoms covered with carbonaceous residues, which in turn enhances conversion of CO to CO_2.[38,39] As the –OH species bind to Ru easier than to Pt, the poisoning is effectively reduced on the surface of Pt catalysts. Therefore, the electrocatalytic oxidation of methanol can be improved if Pt and Ru form an alloy.[31] These results indicate that the new type of metal/carbon nanohybrids reported here has great potential for practical applications in fuel cell electrodes.

CONCLUSIONS

In summary, a synthetic strategy for the fabrication of advanced hybrid metal/carbon nanostructures containing multilayers of dispersed metal nanoparticles in a carbon matrix was introduced. This synthetic strategy involved the combination of layer-by-layer deposition of inverse block copolymer micelles loaded with metal precursor and direct carbonization of the block copolymer. The block copolymer acted as template for the spatial arrangement of the metal nanoparticles and at the same time as carbon source. The self-ordered spatial arrangement of the metal nanoparticles was conserved during carbonization. The obtained metal/carbon nanohybrids containing dispersed noble metal nanoparticles

showed distinct electrocatalytic activity in the oxidation of formic acid and of methanol. By proper selection of the metal precursors, a broad variety of metal/carbon combinations should be accessible that could be utilized in a broad range of energy storage and conversion devices beyond fuel cells.

EXPERIMENTAL SECTION

Materials. All chemicals were used as received without further treatment. Asymmetric poly(styrene-*block*-4-vinyl pyridine) diblock copolymer (PS-*b*-P4VP, $M_{n,PS}$ = 41.5 kg mol^{-1}, $M_{n,P4VP}$ = 17.5 kg mol^{-1}, PDI = 1.07) was purchased from Polymer Source. Platinum chloride ($PtCl_4$), ruthenium chloride ($RuCl_3$), sodium borohydride ($NaBH_4$), perchloric acid ($HClO_4$), and formic acid (HCOOH) were purchased from Sigma Aldrich.

Preparation of Multilayered Pt/Carbon and Pt−Ru/Carbon Electrocatalysts. Pt precursor or mixtures of equal amounts of Pt and Ru precursors (molar ratio 1:1) in isopropyl alcohol (1 wt % of Pt precursor or precursor mixture) were added to solutions of PS-*b*-P4VP in toluene (0.75 wt %) at a molar ratio of metal precursor/vinyl pyridine block = 0.3 and stirred vigorously overnight. Metal/BCP films were prepared on indium tin oxide glass or on Si wafers by spin-coating at 2000 rpm for 60 s using a Spin-1200D (Midas System Inc.) spin-coater and subsequent stabilization by exposure to UV light with a wavelength of 254 nm and a power of 25 W cm^{-2} (XX-15S; UVP, Inc.) for 1 h under vacuum at room temperature. It is well-known that UV irradiation leads to the formation of cross-links in PS as well as PxVP homopolymers.[25,40,41] To form Pt or Pt−Ru nanoparticles, the precursor-loaded inverse micelle films were dipped into an ethanolic $NaBH_4$ solution (0.01 M) for 10 or 30 min followed by washing with ethanol. Experimental details of the fabrication of hybrid carbon nanostructures by direct carbonization are described elsewhere.[26,27] The above procedures were repeated to fabricate metal/BCP multilayer films. Subsequently, direct carbonization of the metal-loaded PS-*b*-P4VP inverse micelle films was carried out by putting the samples into a furnace preheated to 873 K, heating them to this temperature for 1 h in Ar atmosphere, and removing them from the furnace immediately after the heat treatment.

Morphological Analysis. Atomic force microscopy (AFM) of metal/BCP and metal/carbon films was performed with a Digital Instruments Dimension 3100 scanning force microscope in the tapping mode. Top-view TEM images and EDS spectra were obtained on a JEOL JSM-2100-F microscope at 100 kV. The samples for TEM analysis were prepared according to the method described in our previous study.[42] Cross-sectional TEM images were obtained as follows. Al substrates with a diameter of 20.0 mm and a thickness of 0.5 mm (Goodfellow, purity >99.999%) were at first electropolished at room temperature for 4 min at 25 V using a solution of 25 vol% of 60% $HClO_4$ and 75 vol% ethanol. Then, 10 Pt/BCP layers were deposited onto the electropolished Al substrates and carbonized as described above. The Al substrates coated with Pt/BCP10 films were cut into ultrathin slices along a direction perpendicular to the plane of the Pt/BCP10 film using an ultramicrotome Leica UCT and a diamond knife Diatome Ultra 3.0 mm (cutting edge angle 45°). The cutting velocity was 1 mm/s. The slices were transferred to TEM grids (300 mesh) coated with a holey carbon film and investigated on a Zeiss EM902A TEM at 50 kV.

X-ray Reflectivity. To obtain thicknesses (d) and density information, XR measurements on Pt/BCP and Pt/carbon films were performed using a D8 Advanced X-ray diffractometer (Bruker AXS, Germany) equipped with a Cu Kα source (λ = 1.5418 Å). A scintillation detector was combined with a slit with a vertical gap of 0.6 mm.

A series of Pt/BCP samples was prepared on Si wafer pieces with edge lengths of 1.5 cm × 1.5 cm. Since indices of refraction depend on electron density, the indices of refraction of metal/BCP films were sufficiently different from that of the Si substrate. For example, at the incident energy of 8.05 keV of Cu Kα radiation, the calculated indices of refraction $n = 1 - \delta$ of Si, polystyrene (PS), and Pt are $n_{Si} = 1 - 7.5972 \times 10^{-6}$, $n_{PS} = 1 - 3.5579 \times 10^{-6}$ and $n_{Pt} = 1 - 51.893 \times 10^{-6}$, respectively, where δ is the dispersion. As described above, δ linearly depends on the electron density ρ_{el}; the reflected intensity at the interfaces is sensitive to variations in ρ_{el}. If a reflectivity spectrum exhibits a clear periodic oscillation with a period ΔQ_z, the film thickness can readily be estimated from ΔQ_z according to $d = 2\pi/\Delta Q_z$. The recursive *Parratt* formalism was used to fit the measured data by varying the dispersion, the layer thickness, d, and the interfacial roughness of each layer.[43−45]

As seen in Figure 4a,b, XR spectra of Pt/BCP and Pt/carbon films exhibit oscillations with very low amplitude, probably due to the presence of rough surfaces. XR analysis then requires a more vigorous analytic approach; to estimate the absolute density and thickness of a thin film, critical edge regions were carefully observed, as described below.

Essentially, Snell's law of refraction states that an index of refraction n for X-rays crossing the interface between vacuum 1 and a medium 2, is given by

$$n_1 \cos \theta_1 = n_2 \cos \theta_2 \quad (1)$$

where θ_1 and θ_2 are the incident and the reflected angles, respectively, at the interface. For X-ray radiation, the index of refraction can be written as

$$n = 1 - \delta - i\beta \quad (2)$$

The dispersion δ and the absorption β are given by

$$\delta = \lambda^2 \rho_{el} r_0/(2\pi) \quad \text{and} \quad \beta = \mu\lambda/(4\pi) \quad (3)$$

where ρ_{el} is the electron density and $r_0 = 2.8 \times 10^{-10}$ nm is the classical electron radius. For incident angles smaller than a critical minimum value θ_c, total external reflection of the radiation will occur. Combining eqs 1−3, we can derive the relationship between critical wave vector transfer, $Q_{z,c}$, and dispersion by $Q_{z,c} = 4\pi/\lambda(\sin(\theta_c))$, where the critical angle is given by $\theta_c \approx (2\delta)^{1/2}$. Therefore, the exact Q_z positions of the critical edges, where the total external reflection ended, are a clear indication of the presence of the layers having the corresponding dispersions (or the corresponding electron densities). The calculated values for $Q_{z,c}$ at λ = 1.5418 Å for Si, PS, and Pt are 0.03177, 0.02174, and 0.08303 Å^{-1}, respectively.

The expanded reflectivity spectra (inset of Figure 4a) show the intensity at low values of Q_z obtained from samples Pt/BCP1-5 deposited onto Si substrates. For the thinnest sample Pt/BCP1, there is only a single critical edge at 0.03177 Å^{-1} which belongs to the Si substrate, indicating that the presence of a single layer of Pt/BCP1 is not sufficient to generate a critical edge on the top of the Si substrate. A slight dip in intensity progressively developed at $Q_z \approx 0.024$ Å^{-1}, which should correspond to the critical wave vector of BCP multilayers containing Pt. The position of this dip at $Q_{z,c} \approx 0.024$ Å^{-1} is slightly shifted to higher $Q_{z,c}$ values as compared to pure PS-*b*-P4VP ($Q_{z,c}$ = 0.02174 Å^{-1}), revealing that Pt atoms occupy about 4 vol % in Pt/BCP hybrids. The increase in depth of the dip at $Q_{z,c} \approx 0.024$ Å^{-1} associated with deposition of additional metal-containing inverse micelle monolayers indicates an increase in total layer thickness. Combining the faint oscillation from the whole spectrum and the development of the critical Q_z value from the successively deposited Pt/BCP layers, we could estimate the thicknesses of the deposited layers.

Grazing Incidence Small-Angle X-ray Scattering (GISAXS). Two-dimensional (2D)-GISAXS experiments were conducted at 8-ID-E beamlines of the Advanced Photon Source at Argonne National Laboratory, USA, with a wavelength of 1.69 Å ($\Delta\lambda/\lambda = 5 \times 10^{-5}$) and a sample-to-detector distance of 2.2 m. The 2D-GISAXS patterns were recorded by using a 2D detector (DECTRIS Ltd., Pilatus 1M) located at the end of a vacuum guide tube with an

exposure time of 10 s. The scattering vector q^* belonging to an intensity maximum is related to the corresponding d-spacing by $d = 2\pi/q^*$.

X-ray Diffraction and Raman Spectroscopy. Bulk Pt−Ru/carbon and Pt/carbon samples for X-ray diffraction and Raman spectroscopy were prepared by evaporating the solvents from Pt−Ru/BCP and Pt/BCP solutions, followed by cross-linking/reduction/carbonization steps carried out in the same way as in the case of the spin-coated film samples. XRD patterns were obtained with a Rigaku Dmax2000 diffractometer using Ni filtered Cu Kα radiation (λ = 1.5418 Å). Room-temperature micro-Raman scattering spectra were recorded using a McPherson 207 spectrometer equipped with a nitrogen-cooled charge-couple device (CCD) array detector. Light with a wavelength of 488 nm emitted from a DPSS laser was focused to a spot ~1 μm in diameter on the sample surface for 60 s using a microscope objective lens (×100). The excitation laser power on the sample surface was estimated to be 16.5 mW.

X-ray Photoelectron Spectroscopy (XPS). XPS measurements were carried out using monochromatic Al Kα-radiation (Thermo VG, U.K. Al Kα line: 1486.6 eV, 12 kV, 3 mA).

Electrochemical Tests. Cyclic voltammograms were measured in a three-electrode system using a potentiostat (Autolab PGSTAT302N, Eco Chemie) with platinum foil as counter electrode and a Ag/AgCl reference electrode from −0.2 to 1.0 V at a scan rate of 50 mV s^{-1} at room temperature. For the measurements, Pt−Ru/carbon5 and Pt/carbon5 on ITO glasses were used as working electrodes in N_2-saturated aqueous solution of 0.1 M $HClO_4$, or in N_2-saturated mixtures of 0.2 M HCOOH and 0.1 M $HClO_4$ or 0.2 M CH_3OH and 0.1 M $HClO_4$.

Conflict of Interest: The authors declare no competing financial interest.

Supporting Information Available: Additional figures and tables as described in the text. This material is available free of charge *via* the Internet at http://pubs.acs.org.

Acknowledgment. This work was supported by National Research Foundation of Korea Grant funded by the Korean Government (2011-0029409; 2012-0009649; Global Ph.D. Fellowship). D. Y. Ryu acknowledges the partial supports by NRF Grant 2011-0022690 and PAL in Korea. The authors are grateful to B. Walkenfort for his support with the TEM investigations as well as Prof. S. Yoon and H.-Y. Shin for the measurement of Raman spectra.

REFERENCES AND NOTES

1. Vinodgopal, K.; Haria, M.; Meisel, D.; Kamat, P. Fullerene-Based Carbon Nanostructures for Methanol Oxidation. *Nano Lett.* **2004**, *4*, 415–418.
2. Kongkanand, A.; Martínez Domínguez, R.; Kamat, P. V. Single Wall Carbon Nanotube Scaffolds for Photoelectrochemical Solar Cells. Capture and Transport of Photogenerated Electrons. *Nano Lett.* **2007**, *7*, 676–680.
3. Lee, G.; Shim, J. H.; Kang, H.; Nam, K. M.; Song, H.; Park, J. T. Monodisperse Pt and PtRu/C_{60} Hybrid Nanoparticles for Fuel Cell Anode Catalysts. *Chem. Commun.* **2009**, 5036–5038.
4. Yoo, E.; Okata, T.; Akita, T.; Kohyama, M.; Nakamura, J.; Honma, I. Enhanced Electrocatalytic Activity of Pt Subnanoclusters on Graphene Nanosheet Surface. *Nano Lett.* **2009**, *9*, 2255–2259.
5. Stoller, M. D.; Park, S.; Zhu, Y.; An, J.; Ruoff, R. S. Graphene-Based Ultracapacitors. *Nano Lett.* **2008**, *8*, 3498–3502.
6. Liu, L.; Pu, C.; Viswanathan, R.; Fan, Q.; Liu, R.; Smotkin, E. S. Carbon Supported and Unsupported Pt−Ru Anodes for Liquid Feed Direct Methanol Fuel Cells. *Electrochim. Acta* **1998**, *43*, 3657–3663.
7. Steigerwalt, E. S.; Deluga, G. A.; Lukehart, C. M. Pt−Ru/Carbon Fiber Nanocomposites: Synthesis, Characterization, and Performance as Anode Catalysts of Direct Methanol Fuel Cells. A Search for Exceptional Performance. *J. Phys. Chem. B* **2002**, *106*, 760–766.
8. Zhao, G.; He, J.; Zhang, C.; Zhou, J.; Chen, X.; Wang, T. Highly Dispersed Pt Nanoparticles on Mesoporous Carbon Nanofibers Prepared by Two Templates. *J. Phys. Chem. C* **2008**, *112*, 1028–1033.
9. Bessel, C. A.; Laubernds, K.; Rodriguez, N. M.; Baker, R. T. K. Graphite Nanofibers as an Electrode for Fuel Cell Applications. *J. Phys. Chem. B* **2001**, *105*, 1115–1118.
10. Che, G.; Lakshmi, B. B.; Fisher, E. R.; Martin, C. R. Carbon Nanotubule Membranes for Electrochemical Energy Storage and Production. *Nature* **1998**, *393*, 346–349.
11. Chai, G. S.; Yoon, S. B.; Kim, J. H.; Yu, J.-S. Spherical Carbon Capsules with Hollow Macroporous Core and Mesoporous Shell Structures as a Highly Efficient Catalyst Support in the Direct Methanol Fuel Cell. *Chem. Commun.* **2004**, 2766–2767.
12. Joo, S. H.; Choi, S. J.; Oh, I.; Kwak, J.; Liu, Z.; Terasaki, O.; Ryoo, R. Ordered Nanoporous Arrays of Carbon Supporting High Dispersions of Platinum Nanoparticles. *Nature* **2001**, *412*, 169–172.
13. Ji, X.; Lee, K. T.; Holden, R.; Zhang, L.; Zhang, J.; Botton, G. A.; Couillard, M.; Nazar, L. F. Nanocrystalline Intermetallics on Mesoporous Carbon for Direct Formic Acid Fuel Cell Anodes. *Nat. Chem.* **2010**, *2*, 286–293.
14. Fredrickson, G. H.; Bates, F. S. Dynamics of Block Copolymers: Theory and Experiment. *Annu. Rev. Mater. Sci.* **1996**, *26*, 501–550.
15. Hamley, I. W. Ordering in Thin Films of Block Copolymers: Fundamentals to Potential Applications. *Prog. Polym. Sci.* **2009**, *34*, 1161–1210.
16. Bang, J.; Jeong, U.; Ryu, D. Y.; Russell, T. P.; Hawker, C. J. Block Copolymer Nanolithography: Translation of Molecular Level Control to Nanoscale Patterns. *Adv. Mater.* **2009**, *21*, 4769–4792.
17. Möller, M.; Spatz, J. P.; Roescher, A. Gold Nanoparticles in Micellar Poly(styrene)-*b*-Poly(ethylene oxide) Films—Size and Interparticle Distance Control in Monoparticulate Films. *Adv. Mater.* **1996**, *8*, 337–340.
18. Spatz, J. P.; Herzog, T.; Mößmer, S.; Ziemann, P.; Möller, M. Micellar Inorganic−Polymer Hybrid Systems—A Tool for Nanolithography. *Adv. Mater.* **1999**, *11*, 149–153.
19. Han, W.; Byun, M.; Li, B.; Pang, X.; Lin, Z. A Simple Route to Hierarchically Assembled Micelles and Inorganic Nanoparticles. *Angew. Chem., Int. Ed.* **2012**, *51*, 12588–12592.
20. Kowalewski, T.; Tsarevsky, N. V.; Matyjaszewski, K. Nanostructured Carbon Arrays from Block Copolymers of Polyacrylonitrile. *J. Am. Chem. Soc.* **2002**, *124*, 10632–10633.
21. Tang, C.; Tracz, A.; Kruk, M.; Zhang, R.; Smilgies, D.-M.; Matyjaszewski, K.; Kowalewski, T. Long-Range Ordered Thin Films of Block Copolymers Prepared by Zone-Casting and Their Thermal Conversion into Ordered Nanostructured Carbon. *J. Am. Chem. Soc.* **2005**, *127*, 6918–6919.
22. Huang, J.; Tang, C.; Lee, H.; Kowalewski, T.; Matyjaszewski, K. A Novel Route for the Preparation of Discrete Nanostructured Carbons from Block Copolymers with Polystyrene Segments. *Macromol. Chem. Phys.* **2007**, *208*, 2312–2320.
23. Chen, J. T.; Shin, K.; Leiston-Belanger, J. M.; Zhang, M.; Russell, T. P. Amorphous Carbon Nanotubes with Tunable Properties *via* Template Wetting. *Adv. Funct. Mater.* **2006**, *16*, 1476–1480.
24. Ji, X.; Herle, P. S.; Rho, Y.; Nazar, L. F. Carbon/MoO_2 Composite Based on Porous Semi-Graphitized Nanorod Assemblies from *In Situ* Reaction of Tri-Block Polymers. *Chem. Mater.* **2007**, *19*, 374–383.
25. Wang, Y.; Liu, J.; Christiansen, S.; Kim, D. H.; Gösele, U.; Steinhart, M. Nanopatterned Carbon Films with Engineered Morphology by Direct Carbonization of UV-Stabilized Block Copolymer Films. *Nano Lett.* **2008**, *8*, 3993–3997.
26. Jang, Y. H.; Kochuveedu, S. T.; Jang, Y. J.; Shin, H.-Y.; Yoon, S.; Steinhart, M.; Kim, D. H. The Fabrication of Graphitic Thin Films with Highly Dispersed Noble Metal Nanoparticles by Direct Carbonization of Block Copolymer Inverse Micelle Templates. *Carbon* **2011**, *49*, 2120–2126.
27. Kim, D. H. Block Copolymer Nanotemplates as Versatile Platforms for Hybrid Multifunctional Nanostructures. *3rd Intl. Nanoelectr. Conf.* **2010**, 433–434.

28. Yun, S.-H.; Yoo, S. I.; Jung, J. C.; Zin, W.-C.; Sohn, B.-H. Highly Ordered Arrays of Nanoparticles in Large Areas from Diblock Copolymer Micelles in Hexagonal Self-Assembly. *Chem. Mater.* **2006**, *18*, 5646–5648.
29. Roth, C.; Martz, N.; Fuess, H. Characterization of Different Pt−Ru Catalysts by X-ray Diffraction and Transmission Electron Microscopy. *Phys. Chem. Chem. Phys.* **2001**, *3*, 315–319.
30. Ferrari, A. C.; Robertson, J. Interpretation of Raman Spectra of Disordered and Amorphous Carbon. *Phys. Rev. B* **2000**, *61*, 14095–14107.
31. Xu, C.; Wang, R.; Chen, M.; Zhang, Y.; Ding, Y. Dealloying to Nanoporous Au/Pt Alloys and Their Structure Sensitive Electrocatalytic Properties. *Phys. Chem. Chem. Phys.* **2010**, *12*, 239–246.
32. Zhang, S.; Shao, Y.; Yin, G.; Lin, Y. Electrostatic Self-Assembly of a Pt-around-Au Nanocomposite with High Activity Towards Formic Acid Oxidation. *Angew. Chem., Int. Ed.* **2010**, *49*, 2211–2214.
33. Kristian, N.; Yan, Y.; Wang, X. Highly Efficient Submonolayer Pt-Decorated Au Nano-Catalysts for Formic Acid Oxidation. *Chem. Commun.* **2008**, 353–355.
34. Lu, Y.; Chen, W. One-Pot Synthesis of Heterostructured Pt−Ru Nanocrystals for Catalytic Formic Acid Oxidation. *Chem.Commun.* **2011**, *47*, 2541–2543.
35. Jiang, Z.; Jiang, Z.-j. Improvements of Electrocatalytic Activity of PtRu Nanoparticles on Multi-Walled Carbon Nanotubes by a H_2 Plasma Treatment in Methanol and Formic Acid Oxidation. *Electrochim. Acta* **2011**, *56*, 8662–8673.
36. Yu, X.; Pickup, P. G. Recent Advances in Direct Formic Acid Fuel Cells (DFAFC). *J. Power Sources* **2008**, *182*, 124–132.
37. Lemos, S. G.; Oliveira, R. T. S.; Santos, M. C.; Nascente, P. A. P.; Bulhões, L. O. S.; Pereira, E. C. Electrocatalysis of Methanol, Ethanol, and Formic Acid Using a Ru/Pt Metallic Bilayer. *J. Power Sources* **2007**, *163*, 695–701.
38. Park, K.-W.; Choi, J.-H.; Kwon, B.-K.; Lee, S.-A.; Sung, Y.-E.; Ha, H.-Y.; Hong, S.-A.; Kim, H.; Wieckowski, A. Chemical and Electronic Effects of Ni in Pt/Ni and Pt/Ru/Ni Alloy Nanoparticles in Methanol Electrooxidation. *J. Phys. Chem. B* **2002**, *106*, 1869–1877.
39. Long, J. W.; Stroud, R. M.; Swider-Lyons, K. E.; Rolison, D. R. How to Make Electrocatalysts More Active for Direct Methanol Oxidationavoid PtRu Bimetallic Alloys!. *J. Phys. Chem. B* **2000**, *104*, 9772–9776.
40. Harnish, B.; Robinson, J. T.; Pei, Z.; Ramström, O.; Yan, M. UV-Cross-Linked Poly(Vinylpyridine) Thin Films as Reversibly Responsive Surfaces. *Chem. Mater.* **2005**, *17*, 4092–4096.
41. Yan, M.; Harnish, B. A Simple Method for the Attachment of Polymer Films on Solid Substrates. *Adv. Mater.* **2003**, *15*, 244–248.
42. Jang, Y. J.; Kim, D. H. One-Step and Self-Assembly Based Fabrication of Pt/TiO_2 Nanohybrid Photocatalysts with Programmed Nanopatterns. *Chem.—Eur. J.* **2011**, *17*, 540–545.
43. Tolan, M. *X-ray Scattering from Soft-Matter Thin Films;* Springer Tracts in Modern Physics, Vol. 148; Springer: Berlin, 1999.
44. Russell, T. P. X-ray and Neutron Reflectivity for the Investigation of Polymers. *Mater. Sci. Rep.* **1990**, *5*, 171–271.
45. Sun, Y.; Frenkel, A. I.; Isseroff, R.; Shonbrun, C.; Forman, M.; Shin, K.; Koga, T.; White, H.; Zhang, L.; Zhu, Y.; *et al.* Characterization of Palladium Nanoparticles by Using X-ray Reflectivity, EXAFS, and Electron Microscopy. *Langmuir* **2006**, *22*, 807–816.